




Loss-induced Floquet non-Hermitian skin effectYaohua Li ¹, Cuicui Lu ^{2,3}, Shuang Zhang ³, and Yong-Chun Liu ^{1,4,*}¹State Key Laboratory of Low-Dimensional Quantum Physics, Department of Physics, Tsinghua University, Beijing 100084, China²Key Laboratory of Advanced Optoelectronic Quantum Architecture and Measurements of Ministry of Education, Beijing Key Laboratory of Nanophotonics and Ultrafine Optoelectronic Systems, School of Physics, Beijing Institute of Technology, Beijing 100081, China³Department of Physics, University of Hong Kong, Hong Kong 999077, China⁴Frontier Science Center for Quantum Information, Beijing 100084, China

(Received 31 May 2023; revised 29 October 2023; accepted 17 November 2023; published 12 December 2023)

Non-Hermitian topological systems have attracted much interest due to their unique topological properties when the non-Hermitian skin effect (NHSE) appears. However, the experimental realization of NHSE conventionally requires nonreciprocal couplings, which are compatible with limited systems. Here, we propose a mechanism of loss-induced Floquet NHSE, where the loss provides the basic source of non-Hermiticity and the Floquet engineering brings about Floquet-induced complex next-nearest-neighbor couplings. We also extend the generalized Brillouin zone theory to nonequilibrium systems to describe the Floquet NHSE. Furthermore, we show that this mechanism can realize the second-order NHSE when generalized to two-dimensional systems. Our proposal can be realized in photonic lattices with helical waveguides and other related systems, which opens the door for the study of topological phases in Floquet non-Hermitian systems.

DOI: [10.1103/PhysRevB.108.L220301](https://doi.org/10.1103/PhysRevB.108.L220301)

Introduction. Non-Hermitian systems exhibit rich topological phases that are characterized by non-Hermitian topological invariants [1–6]. One of their unique features is the appearance of the non-Hermitian skin effect (NHSE) [7–17], which leads to the breakdown of conventional bulk-boundary correspondence and the introduction of a generalized Brillouin zone (GBZ) [18–23], and shows wide applications such as chiral damping or amplification [24] and anomalous lasing [25]. The NHSE has also been extended to higher-dimensional topological systems with the emergence of the hybrid skin-topological effect, where the topological edge states are further localized into the corners [26,27], and it is a kind of higher-order NHSE [28] originating from the non-trivial interplay between the NHSE and the topological effect.

Recently, the NHSE has been observed in photonic systems [29], acoustic systems [30,31], electrical circuits [32,33], and through quantum dynamics [34]. However, all these realizations require nonreciprocal couplings, which are not applicable in a large variety of systems without nonreciprocity. At the same time, another mechanism through the gain/loss is proposed, where the amplifying and dissipative behaviors of the chiral current along different edges lead to the NHSE [8,14,27], but the generation of the chiral edge current requires complex next-nearest-neighbor couplings, which is difficult to implement in experiments.

On the other hand, topological phases have also been extended into periodically driven systems, known as Floquet topological insulators [35–42]. The Hamiltonians of those systems are periodic in time, offering the opportunity to engineer the band structure in the quasienergy spectrum. The

Floquet topological phases have shown great success in experiments [43–48], including the realization of a photonic topological phase [49] and the Haldane model [50]. Recently, there are growing efforts in studying the non-Hermitian topological phase transitions in nonequilibrium systems [51–57]. It is proposed that Floquet engineering can be used to generate nonreciprocal couplings and then induce the NHSE [58]. An anomalous Floquet NHSE is found in the ring resonator lattice which supports two circulation sectors that are each effectively nonreciprocal [59]. However, the relation between the Floquet driving and the loss-induced NHSE remains unknown.

In this Letter, we uncover the mechanism of loss-induced Floquet NHSE, where gain/loss combined with Floquet engineering leads to the NHSE. Here, gain/loss provides the origin of non-Hermiticity, while Floquet engineering plays a crucial role in generating the chiral current through Floquet-induced next-nearest-neighbor couplings. To describe the Floquet NHSE, we also extend the generalized Brillouin zone theory to nonequilibrium systems. Our proposal reveals a general mechanism to realize the NHSE, and we show it can be extended to two dimensions to generate both first- and second-order non-Hermitian skin effects. Importantly, our mechanism does not rely on the Floquet topology. Except for the second-order skin-topological effect, the first-order NHSE can be directly generated by Floquet-induced next-nearest-neighbor couplings even when the Floquet system remains trivial.

Floquet non-Hermitian skin effect. We first consider a Floquet non-Hermitian photonic lattice, as illustrated in Fig. 1(a). It is a one-dimensional zigzag array of helical waveguides. The helical radius is R , and the pitch is Z . There are two waveguides in each unit cell, where one of

*ycliu@tsinghua.edu.cn

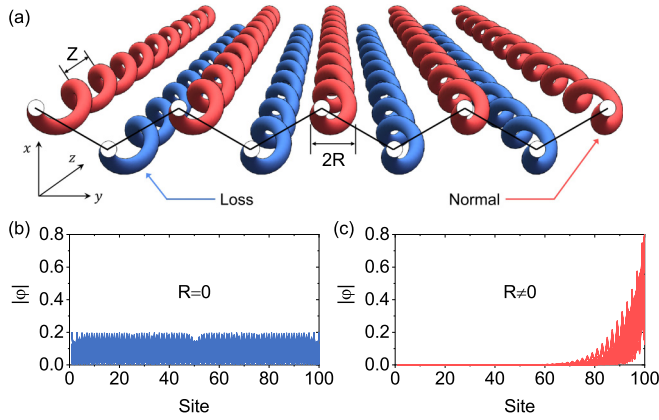


FIG. 1. (a) Sketch of the non-Hermitian helical waveguides. The waveguides point to the z direction and are arranged in a zigzag structure along the y direction. There are two kinds of waveguides: the normal waveguides in red and the lossy waveguides in blue. The helical radius is R , and the pitch is Z . (b), (c) The profile of all the eigenstates of the effective coupling matrix when (b) $R = 0$ and (c) $R = 10 \mu\text{m}$. There is no non-Hermitian skin effect for $R = 0$ and there is the non-Hermitian skin effect towards the right for $R \neq 0$. The distance between two nearest-neighbor waveguides is $a = 15 \mu\text{m}$. Other parameters are $Z = 1 \text{ cm}$, $k_0/2\pi = 2.4 \mu\text{m}^{-1}$, $c = 1 \text{ cm}^{-1}$, $\gamma = 0.8 \text{ cm}^{-1}$.

them is lossy and the other is normal, which is also similar to the case of two waveguides with different losses. The loss in the waveguide can be achieved, for example, by replacing the continuous waveguide with periodic waveguide sections that have the same helical pattern. This photonic lattice can be well described by a tight-binding model with nearest-neighbor couplings, and the coupled equations can be written as [49]

$$i\partial_z \psi_n(z) = -i\gamma_n \psi_n(z) + \sum_{m=n\pm 1} c e^{i\mathbf{A}(z)\cdot\mathbf{r}_{mn}} \psi_m(z), \quad (1)$$

where $\psi_n(z)$ (γ_n) is the amplitude (loss) of the n th waveguide, c is the coupling strength, and \mathbf{r}_{mn} is the displacement between waveguides m and n . Here, we assume $\gamma_n = 2\gamma$ for all the lossy waveguides, while the normal waveguides have zero loss. After neglecting a global loss term $-i\gamma\psi_n$, Eq. (1) becomes the coupling equations of a non-Hermitian system with balanced gain and loss. $\mathbf{A}(z) = k_0 R \Omega (-\cos \Omega z, \sin \Omega z, 0)$ is a z -dependent vector potential induced by the helical shape of the waveguides, where k_0 is the wave number, and $\Omega = 2\pi/Z$ is the frequency of the rotation.

We can rewrite the coupled equations as $i\partial_z \boldsymbol{\psi}(z) = H(z)\boldsymbol{\psi}(z)$, where $\boldsymbol{\psi}(z) = (\psi_1, \psi_2, \dots)^T$ is the amplitude vector, and $H(z)$ is the non-Hermitian coupling matrix. The propagation of light along the waveguides can simulate the evolution of the single-particle Schrödinger equations, where the spatial dimension z plays the role of the time dimension and the coupling matrix is an analog of the quantum Hamiltonian. The coupling matrix is z dependent and has a period Z : $H(z) = H(z+Z)$. So there are no static solutions for the coupling equations. Instead, the solutions can be expressed in terms of the Floquet states, $|\boldsymbol{\psi}(z)\rangle = e^{-i\varepsilon z} |\boldsymbol{\Phi}(z)\rangle$, with $|\boldsymbol{\Phi}(z)\rangle = |\boldsymbol{\Phi}(z+Z)\rangle$, and ε is the quasienergy. The Floquet

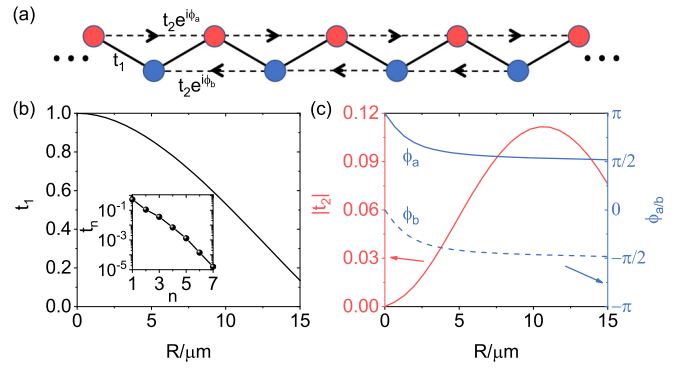


FIG. 2. (a) Effective coupling structure of the helical waveguides considering the nearest-neighbor (solid lines) and next-nearest-neighbor (dotted lines) couplings. The red (blue) circles denote the normal and lossy waveguides, while the arrows indicate the phases of the next-nearest-neighbor couplings. (b) The amplitude of the effective nearest-neighbor coupling. The inset is the amplitudes of the long-range couplings as a function of the distance n . (c) The amplitudes (red lines) and phases (blue lines) of the effective next-nearest-neighbor couplings. The coupling phases between normal (blue solid line) and loss (blue dotted line) waveguides have opposite signs, corresponding to the opposite arrow directions in (a). These results are obtained in the Hermitian case without loss. Other parameters are the same as in Fig. 1.

states are the eigenstates of the Floquet operator, i.e., the evolution operator of a full period, $U(Z) = \mathcal{F} \exp[-i \int_0^Z H(z) dz]$ (\mathcal{F} denotes the spatial order along the z axis). From the Floquet operator, we can define the effective coupling matrix H_{eff} that satisfied $U(Z) = \exp(-iH_{\text{eff}}Z)$ [60].

Figures 1(b) and 1(c) are the profiles of all the eigenstates of the effective coupling matrix when $R = 0$ and $R \neq 0$. In the former case with straight waveguides ($R = 0$), the system reduces to a trivial chain with static nearest-neighbor couplings. The coupling matrix satisfies $(\mathcal{PT})^{-1}H\mathcal{PT}$ after neglecting the global loss, where \mathcal{P} is the mapping from the left side to the right side, and \mathcal{T} is the complex conjugation. In this case, the NHSE is forbidden by the \mathcal{PT} symmetry [Fig. 1(b)], because any eigenstate that is localized at one side will be mapped into the other side after the \mathcal{PT} operation. On the contrary, the helical waveguides introduce a chiral potential encoded in the coupling phases and break the \mathcal{PT} symmetry. As shown in Fig. 1(c), the system with helical waveguides ($R \neq 0$) exhibits the NHSE with all the eigenstates located at the right boundary. The NHSE is obtained through Floquet-engineered couplings accompanied by non-Hermiticity from gain/loss, which does not require nonreciprocal couplings.

Effective coupling structure. To reveal the physics of the Floquet NHSE, we calculate the average strengths and phases of the couplings in the effective coupling matrix H_{eff} . Figure 2(a) is the sketch of the effective coupling structure, where t_n denotes the n th-nearest-neighbor couplings. As shown in the inset of Fig. 2(b), the coupling strength is exponentially related to the distance n . Consequently, we can neglect other long-range couplings except for the leading two orders, i.e., the nearest-neighbor couplings t_1 [Fig. 2(b)] and the next-nearest-neighbor couplings t_2 [Fig. 2(c)]. In this case, the

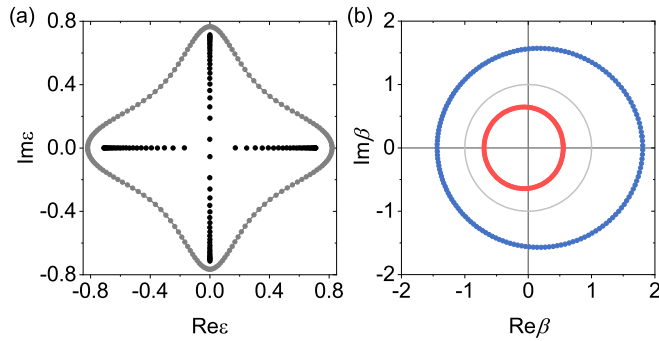


FIG. 3. (a) The spectra of the photonic lattice with helical waveguides in the periodic boundary condition (gray dots) and the open boundary condition (black dots). (b) The generalized Brillouin zone of the system for $\gamma = 0.8 \text{ cm}^{-1}$ (blue dots) and $\gamma = -0.8 \text{ cm}^{-1}$ (red dots). The gray line is a unit circle at the origin. The helical radius is $R = 10 \text{ }\mu\text{m}$. Other parameters are the same as in Fig. 1.

effective coupling equations can be approximately written as

$$i\partial_{z'}\psi_n(z') \approx -i\gamma'_n\psi_n(z') + t_1\psi_{n-1}(z') + t_1\psi_{n+1}(z') + t_2e^{i\phi_{2,n}}\psi_{n+2}(z') + t_2e^{-i\phi_{2,n}}\psi_{n-2}(z'), \quad (2)$$

where γ'_n is the effective loss, and $z' = z/Z$ is the dimensionless coordinate. Here, we have absorbed the coupling phases of the nearest-neighbor couplings t_1 into the mode amplitudes $\psi_n(z')$. It is a coupling equation describing a static system with the same coupling structure in the effective coupling matrix (neglecting the long-range couplings for $n > 2$). When $R \rightarrow 0$, the effective nearest-neighbor coupling strength is $t_1 = cZ$, corresponding to the static photon tunneling strength between nearby waveguides. As shown in Fig. 2(b), the effective nearest-neighbor coupling strength decreases when increasing the helical radius, due to the emergence of long-range photon tunnelings. Among these long-range couplings, the next-nearest-neighbor couplings play the most important role in the Floquet non-Hermitian skin effect. Due to the chiral potential in the original periodic coupling, the effective next-nearest-neighbor couplings between normal and lossy waveguides, i.e., the upper and lower dotted lines in Fig. 2(a), possess coupling phases with opposite signs. Letting the average values of two coupling phases be $\bar{\phi}_{2,n} = \phi_{a(b)}$ for $n \in \text{odd}(\text{even})$, we can obtain the two coupling phases as shown in Fig. 2(c). The blue solid (dotted) line denotes the coupling phase between the normal (loss) waveguides. This asymmetry only exists in the zigzag chain and will disappear when the waveguides are arranged along a straight line. The asymmetric coupling phases can induce the chiral edge current, which is the key requirement of the gain-loss-induced NHSE [8,14,27]. Since the chiral edge current is independent on the loss, in the calculation of effective coupling coefficients (Fig. 2) we consider the Hermitian case without loss. In an intuitive picture, the combination of loss and multichannel interference with a controllable phase from the Floquet coupling effectively generates nonreciprocal couplings [61], which result in the NHSE.

Floquet generalized Brillouin zone. In the periodic boundary condition along both x and y directions, the k -space coupling matrix is given by $\mathcal{H}_k(z) = h_1(z)\sigma_x + h_2(z)\sigma_y +$

$i\gamma(\sigma_z - I)$, where $\sigma_{x,y,z}$ are the Pauli matrices, I is the identity matrix, and the global loss term $-i\gamma I$ can be neglected as it does not affect the detailed band structure. The coefficients $h_{1,2}$ are

$$h_1 = c \cos[\mathbf{A} \cdot \mathbf{a}_1] + c \cos[\mathbf{A} \cdot \mathbf{a}_2 - \sqrt{3}ka], \quad (3)$$

$$h_2 = -c \sin[\mathbf{A} \cdot \mathbf{a}_1] - c \sin[\mathbf{A} \cdot \mathbf{a}_2 - \sqrt{3}ka], \quad (4)$$

where k is the wave vector, $\mathbf{a}_1 = a(-\sin \pi/6, \cos \pi/6)$, $\mathbf{a}_2 = a(-\sin \pi/6, -\cos \pi/6)$, and a is the distance between the nearest-neighbor waveguides. In Fig. 3(a), we plot the quasienergy spectrum in the periodic boundary condition (gray dots), which forms a loop in the complex plane. The spectrum of a finite lattice (black dots) lies in the interior of the loop. It indicates the existence of the NHSE and the failure of the conventional band theory with the Bloch Hamiltonian [13]. To recover the real-space spectrum, we extend the GBZ theory developed in static systems to nonequilibrium systems. The basic idea of GBZ is the replacement $e^{ik} \rightarrow \beta$ in the Bloch Hamiltonian to include the exponential distribution of eigenstates due to the NHSE. For example, here the k -space coupling matrix can be rewritten as (with the replacement $e^{\sqrt{3}ika} \rightarrow \beta$)

$$H_\beta(z) = \begin{pmatrix} 0 & ce^{-i\mathbf{A} \cdot \mathbf{a}_1} + ce^{-i\mathbf{A} \cdot \mathbf{a}_2} \beta^{-1} \\ ce^{i\mathbf{A} \cdot \mathbf{a}_1} + ce^{i\mathbf{A} \cdot \mathbf{a}_2} \beta & -2i\gamma \end{pmatrix}. \quad (5)$$

In the presence of the NHSE, the eigenstates have exponential profiles instead of being equally distributed. Consequently, the bulk states cannot be transformed into a series of plane waves. The above replacement can solve the problem by adding a decay or growing factor. The absolute value of β , i.e., the GBZ, can be unequal to unity, and it corresponds to the exponential behavior of the eigenstates' distributions. The eigenstates will be localized rightwards (positive direction) for $|\beta| > 1$ and leftwards (negative direction) for $|\beta| < 1$. In static two-band systems, the GBZ can be obtained by solving the characteristic equation $f(\beta, E) = \det[E - H(\beta)] = 0$ under the condition that the two specific solutions $\beta_{1,2}$ satisfy $|\beta_1| = |\beta_2|$. To obtain the GBZ in the nonequilibrium system, we need to solve the characteristic equation of the effective coupling matrix, $f_e(\beta, E) = \det[E - H_{\text{eff}}(\beta)] = 0$, which, however, is inaccessible as the effective coupling matrix can only be numerically obtained. Instead, we calculate the GBZ by changing the absolute value of β for a fixed argument and searching the eigenvalues with pure real or imaginary values. In this case, we can obtain the GBZ that recovers the real-space spectrum. Moreover, we check that all the GBZ obtained by this method satisfies $f(\beta_0, E_0) = 0 = f(\beta_0^*, E_0)$. As shown in Fig. 3(b), when $\gamma > 0$ (blue lines), the GBZ lies on the outside of the unit circle, corresponding to the NHSE with rightwards localization [see Fig. 1(c)]. On the contrary, when $\gamma < 0$ (red lines), the GBZ lies on the inside of the unit circle, corresponding to the leftwards localization.

Two-dimensional generalizations. Here, we show that the mechanism of loss-induced Floquet NHSE can be generalized to two-dimensional systems. Remarkably, rich phenomena including the first-order NHSE and the second-order skin-topological effect can be realized. As shown in Fig. 4(a), we

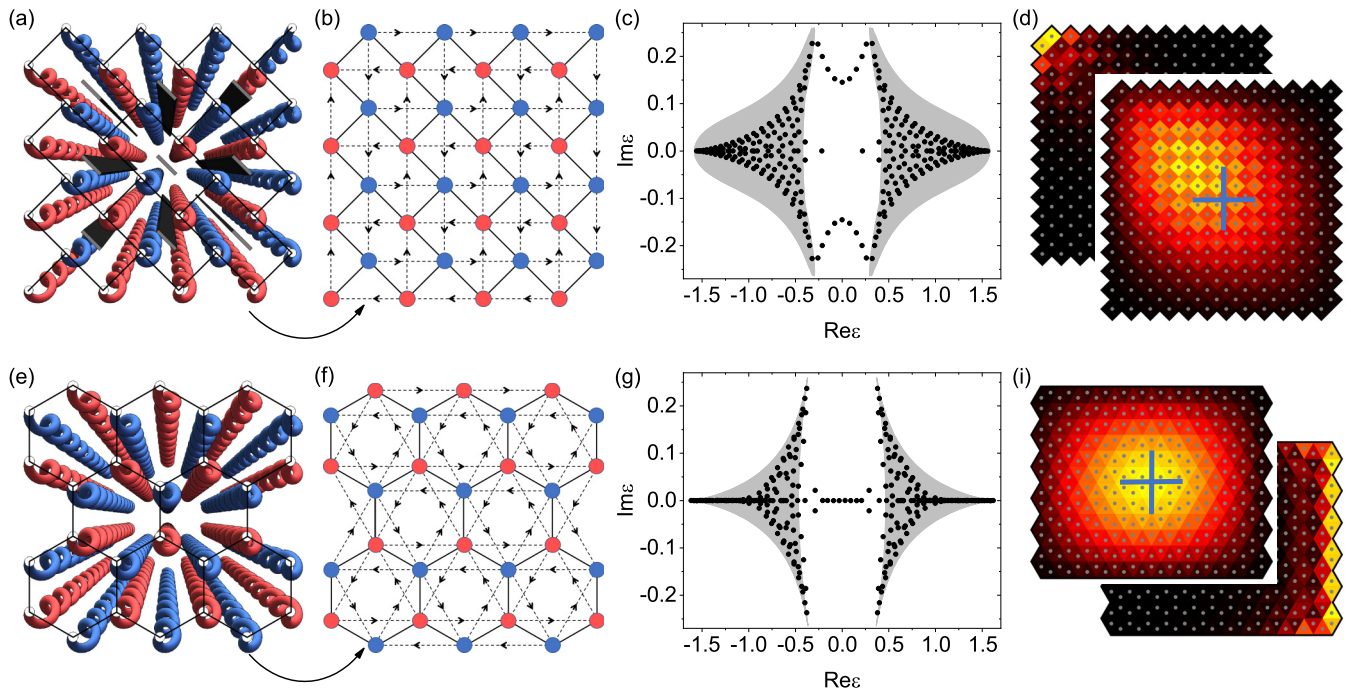


FIG. 4. Two-dimensional non-Hermitian skin effects in [(a)–(d)] the two-dimensional zigzag array and [(e)–(i)] the honeycomb array. (a), (e) Sketches of the two structures. (b), (f) Effective coupling structures. (c), (g) Quasienergy spectra in the periodic (gray areas) and open (black dots) boundary conditions. (d), (i) Profiles of the bulk states (upper figures) and the edge states (lower figures) normalized by the maximal value. The blue crosses indicate the centers of the rectangles. The loss in the blue waveguides is $\gamma = 0.3 \text{ cm}^{-1}$, and the helical radius is $R = 10 \text{ }\mu\text{m}$. Other parameters are the same as in Fig. 1.

first consider a two-dimensional array of helical waveguides, which is a mesh of two zigzag models in both horizontal and vertical directions. In order to take into account of the interplay between the topology and the non-Hermiticity, we consider that there are several plates which prevent the couplings between special waveguides as plotted in Fig. 4(a). The effective coupling structure considering the first two orders of coupling is shown in Fig. 4(b), where the arrows denote the coupling phases. Without the losses, the effective static model in Fig. 4(b) has a similar phase diagram of the Haldane model, with topological phase transitions driven by the next-nearest-neighbor coupling phases and on-site energies (see the Supplemental Material [60] for more details). The Floquet-induced next-nearest-neighbor couplings can open a topological band gap with the emergence of robust chiral edge states. In the presence of losses, the spectra in the periodic boundary conditions (gray area) and open boundary conditions (black dots) are very different, as plotted in Fig. 4(c), which reveals the existence of NHSE. As shown in Fig. 4(d), both the bulk states and the edge states exhibit localization towards the corner, which represents the first-order NHSE in two dimensions. A larger loss γ leads to a clearer localization behavior (see the Supplemental Material [60] for more details). We note that the additional plates that block the couplings between specific waveguides are essential for the introduction of the topology, but the first-order NHSE is independent on the topology and still exists without the additional plates.

In Fig. 4(e), we further consider a honeycomb array of helical waveguides. As shown in Fig. 4(f), the Floquet-induced next-nearest-neighbor couplings have coupling phases that exactly match those in the Haldane model. Consequently, the honeycomb array can realize an effective non-Hermitian Haldane model, and thus we can obtain the second-order skin-topological effect [27]. In this case, only the topological edge states exhibit the NHSE, while the bulk states remain extended with the same distribution as the Hermitian case [Fig. 4(i)]. In the presence of the second-order skin-topological effect, the conventional bulk-boundary correspondence is still valid, which can be characterized by the non-Hermitian Chern number. We obtain the phase diagram of the model and show that the skin-topological phase exists approximately when the loss parameter γ is smaller than the effective nearest-neighbor coupling coefficient t_1 (see the Supplemental Material [60] for more details).

Conclusion. In summary, we have proposed the mechanism of loss-induced Floquet NHSE. The NHSE originates from a combination of gain/loss and the Floquet-induced next-nearest-neighbor couplings. We extend the generalized Brillouin zone theory from static systems to nonequilibrium systems and show it can solve the failure of conventional band theory with Bloch Hamiltonians. Moreover, we show that such a mechanism can also be used to generate both the first-order and second-order NHSE in two dimensions based on different lattice structures. The first-order NHSE is similar to that in one dimension, which is independent from the system topology. As for the second-order skin-topological

effect, we show the Floquet driving can perfectly reveal the phase diagram characterized by the non-Hermitian Chern numbers. Our proposal paves the way for the investigation of non-Hermitian physics in Floquet systems and gain/loss systems.

Note added. Recently, we became aware of a related work [62].

Acknowledgments. This work is supported by the National Key R&D Program of China (Grant No. 2023YFA1407600), the Key-Area Research and Development Program of Guangdong Province (Grant No. 2019B030330001), and the National Natural Science Foundation of China (NSFC) (Grants No. 12275145, No. 92050110, No. 91736106, No. 11674390, and No. 91836302).

-
- [1] Y. Ashida, Z. Gong, and M. Ueda, Non-Hermitian physics, *Adv. Phys.* **69**, 249 (2020).
- [2] T. Liu, Y.-R. Zhang, Q. Ai, Z. Gong, K. Kawabata, M. Ueda, and F. Nori, Second-order topological phases in non-Hermitian systems, *Phys. Rev. Lett.* **122**, 076801 (2019).
- [3] X.-W. Luo and C. Zhang, Higher-order topological corner states induced by gain and loss, *Phys. Rev. Lett.* **123**, 073601 (2019).
- [4] K. Kawabata, K. Shiozaki, M. Ueda, and M. Sato, Symmetry and topology in non-Hermitian physics, *Phys. Rev. X* **9**, 041015 (2019).
- [5] B. Hu, Z. Zhang, H. Zhang, L. Zheng, W. Xiong, Z. Yue, X. Wang, J. Xu, Y. Cheng, X. Liu, and J. Christensen, Non-Hermitian topological whispering gallery, *Nature (London)* **597**, 655 (2021).
- [6] K. Wang, A. Dutt, C. C. Wojcik, and S. Fan, Topological complex-energy braiding of non-Hermitian bands, *Nature (London)* **598**, 59 (2021).
- [7] X. Zhang, T. Zhang, M.-H. Lu, and Y.-F. Chen, A review on non-Hermitian skin effect, *Adv. Phys.: X* **7**, 2109431 (2022).
- [8] T. E. Lee, Anomalous edge state in a non-Hermitian lattice, *Phys. Rev. Lett.* **116**, 133903 (2016).
- [9] S. Yao, F. Song, and Z. Wang, Non-Hermitian Chern bands, *Phys. Rev. Lett.* **121**, 136802 (2018).
- [10] F. Song, S. Yao, and Z. Wang, Non-Hermitian topological invariants in real space, *Phys. Rev. Lett.* **123**, 246801 (2019).
- [11] D. S. Borgnia, A. J. Kruchkov, and R.-J. Slager, Non-Hermitian boundary modes and topology, *Phys. Rev. Lett.* **124**, 056802 (2020).
- [12] N. Okuma, K. Kawabata, K. Shiozaki, and M. Sato, Topological origin of non-Hermitian skin effects, *Phys. Rev. Lett.* **124**, 086801 (2020).
- [13] K. Zhang, Z. Yang, and C. Fang, Correspondence between winding numbers and skin modes in non-Hermitian systems, *Phys. Rev. Lett.* **125**, 126402 (2020).
- [14] Y. Yi and Z. Yang, Non-Hermitian skin modes induced by on-site dissipations and chiral tunneling effect, *Phys. Rev. Lett.* **125**, 186802 (2020).
- [15] C.-X. Guo, C.-H. Liu, X.-M. Zhao, Y. Liu, and S. Chen, Exact solution of non-Hermitian systems with generalized boundary conditions: Size-dependent boundary effect and fragility of the skin effect, *Phys. Rev. Lett.* **127**, 116801 (2021).
- [16] S. Longhi, Self-healing of non-Hermitian topological skin modes, *Phys. Rev. Lett.* **128**, 157601 (2022).
- [17] K. Zhang, Z. Yang, and C. Fang, Universal non-Hermitian skin effect in two and higher dimensions, *Nat. Commun.* **13**, 2496 (2022).
- [18] S. Yao and Z. Wang, Edge states and topological invariants of non-Hermitian systems, *Phys. Rev. Lett.* **121**, 086803 (2018).
- [19] K. Yokomizo and S. Murakami, Non-Bloch band theory of non-Hermitian systems, *Phys. Rev. Lett.* **123**, 066404 (2019).
- [20] Z. Yang, K. Zhang, C. Fang, and J. Hu, Non-Hermitian bulk-boundary correspondence and auxiliary generalized Brillouin zone theory, *Phys. Rev. Lett.* **125**, 226402 (2020).
- [21] C. H. Lee and R. Thomale, Anatomy of skin modes and topology in non-Hermitian systems, *Phys. Rev. B* **99**, 201103(R) (2019).
- [22] C. H. Lee, L. Li, R. Thomale, and J. Gong, Unraveling non-Hermitian pumping: Emergent spectral singularities and anomalous responses, *Phys. Rev. B* **102**, 085151 (2020).
- [23] X. Zhang, G. Li, Y. Liu, T. Tai, R. Thomale, and C. H. Lee, Tidal surface states as fingerprints of non-Hermitian nodal knot metals, *Commun. Phys.* **4**, 47 (2021).
- [24] F. Song, S. Yao, and Z. Wang, Non-Hermitian skin effect and chiral damping in open quantum systems, *Phys. Rev. Lett.* **123**, 170401 (2019).
- [25] B. Zhu, Q. Wang, D. Leykam, H. Xue, Q. J. Wang, and Y. D. Chong, Anomalous single-mode lasing induced by nonlinearity and the non-Hermitian skin effect, *Phys. Rev. Lett.* **129**, 013903 (2022).
- [26] C. H. Lee, L. Li, and J. Gong, Hybrid higher-order skin-topological modes in nonreciprocal systems, *Phys. Rev. Lett.* **123**, 016805 (2019).
- [27] Y. Li, C. Liang, C. Wang, C. Lu, and Y.-C. Liu, Gain-loss-induced hybrid skin-topological effect, *Phys. Rev. Lett.* **128**, 223903 (2022).
- [28] K. Kawabata, M. Sato, and K. Shiozaki, Higher-order non-Hermitian skin effect, *Phys. Rev. B* **102**, 205118 (2020).
- [29] S. Weidemann, M. Kremer, T. Helbig, T. Hofmann, A. Stegmaier, M. Greiter, R. Thomale, and A. Szameit, Topological funneling of light, *Science* **368**, 311 (2020).
- [30] L. Zhang, Y. Yang, Y. Ge, Y.-J. Guan, Q. Chen, Q. Yan, F. Chen, R. Xi, Y. Li, D. Jia, S.-Q. Yuan, H.-X. Sun, H. Chen, and B. Zhang, Acoustic non-Hermitian skin effect from twisted winding topology, *Nat. Commun.* **12**, 6297 (2021).
- [31] X. Zhang, Y. Tian, J.-H. Jiang, M.-H. Lu, and Y.-F. Chen, Observation of higher-order non-Hermitian skin effect, *Nat. Commun.* **12**, 5377 (2021).
- [32] T. Helbig, T. Hofmann, S. Imhof, M. Abdelghany, T. Kiessling, L. W. Molenkamp, C. H. Lee, A. Szameit, M. Greiter, and R. Thomale, Generalized bulk-boundary correspondence in non-Hermitian topoelectrical circuits, *Nat. Phys.* **16**, 747 (2020).
- [33] D. Zou, T. Chen, W. He, J. Bao, C. H. Lee, H. Sun, and X. Zhang, Observation of hybrid higher-order skin-topological effect in non-Hermitian topoelectrical circuits, *Nat. Commun.* **12**, 7201 (2021).

- [34] L. Xiao, T. Deng, K. Wang, G. Zhu, Z. Wang, W. Yi, and P. Xue, Non-Hermitian bulk-boundary correspondence in quantum dynamics, *Nat. Phys.* **16**, 761 (2020).
- [35] J. Cayssol, B. Dóra, F. Simon, and R. Moessner, Floquet topological insulators, *Phys. Status Solidi RRL* **7**, 101 (2013).
- [36] T. Kitagawa, E. Berg, M. Rudner, and E. Demler, Topological characterization of periodically driven quantum systems, *Phys. Rev. B* **82**, 235114 (2010).
- [37] N. H. Lindner, G. Refael, and V. Galitski, Floquet topological insulator in semiconductor quantum wells, *Nat. Phys.* **7**, 490 (2011).
- [38] L. Jiang, T. Kitagawa, J. Alicea, A. R. Akhmerov, D. Pekker, G. Refael, J. I. Cirac, E. Demler, M. D. Lukin, and P. Zoller, Majorana fermions in equilibrium and in driven cold-atom quantum wires, *Phys. Rev. Lett.* **106**, 220402 (2011).
- [39] M. S. Rudner, N. H. Lindner, E. Berg, and M. Levin, Anomalous edge states and the bulk-edge correspondence for periodically driven two-dimensional systems, *Phys. Rev. X* **3**, 031005 (2013).
- [40] A. G. Grushin, A. Gómez-León, and T. Neupert, Floquet fractional Chern insulators, *Phys. Rev. Lett.* **112**, 156801 (2014).
- [41] R. Fleury, A. B. Khanikaev, and A. Alù, Floquet topological insulators for sound, *Nat. Commun.* **7**, 11744 (2016).
- [42] H. Hu, B. Huang, E. Zhao, and W. V. Liu, Dynamical singularities of Floquet higher-order topological insulators, *Phys. Rev. Lett.* **124**, 057001 (2020).
- [43] N. Fläschner, B. S. Rem, M. Tarnowski, D. Vogel, D.-S. Lühmann, K. Sengstock, and C. Weitenberg, Experimental reconstruction of the Berry curvature in a Floquet Bloch band, *Science* **352**, 1091 (2016).
- [44] Y.-G. Peng, C.-Z. Qin, D.-G. Zhao, Y.-X. Shen, X.-Y. Xu, M. Bao, H. Jia, and X.-F. Zhu, Experimental demonstration of anomalous Floquet topological insulator for sound, *Nat. Commun.* **7**, 13368 (2016).
- [45] L. J. Maczewsky, J. M. Zeuner, S. Nolte, and A. Szameit, Observation of photonic anomalous Floquet topological insulators, *Nat. Commun.* **8**, 13756 (2017).
- [46] J. W. McIver, B. Schulte, F.-U. Stein, T. Matsuyama, G. Jotzu, G. Meier, and A. Cavalleri, Light-induced anomalous Hall effect in graphene, *Nat. Phys.* **16**, 38 (2020).
- [47] K. Wintersperger, C. Braun, F. N. Únal, A. Eckardt, M. D. Liberto, N. Goldman, I. Bloch, and M. Aidelsburger, Realization of an anomalous Floquet topological system with ultracold atoms, *Nat. Phys.* **16**, 1058 (2020).
- [48] Z. Zhang, P. Delplace, and R. Fleury, Superior robustness of anomalous non-reciprocal topological edge states, *Nature (London)* **598**, 293 (2021).
- [49] M. C. Rechtsman, J. M. Zeuner, Y. Plotnik, Y. Lumer, D. Podolsky, F. Dreisow, S. Nolte, M. Segev, and A. Szameit, Photonic Floquet topological insulators, *Nature (London)* **496**, 196 (2013).
- [50] G. Jotzu, M. Messer, R. Desbuquois, M. Lebrat, T. Uehlinger, D. Greif, and T. Esslinger, Experimental realization of the topological Haldane model with ultracold fermions, *Nature (London)* **515**, 237 (2014).
- [51] L. Zhou and J. Gong, Non-Hermitian Floquet topological phases with arbitrarily many real-quasienergy edge states, *Phys. Rev. B* **98**, 205417 (2018).
- [52] B. Höckendorf, A. Alvermann, and H. Fehske, Non-Hermitian boundary state engineering in anomalous Floquet topological insulators, *Phys. Rev. Lett.* **123**, 190403 (2019).
- [53] L. Zhou, Dynamical characterization of non-Hermitian Floquet topological phases in one dimension, *Phys. Rev. B* **100**, 184314 (2019).
- [54] X. Zhang and J. Gong, Non-Hermitian Floquet topological phases: Exceptional points, coalescent edge modes, and the skin effect, *Phys. Rev. B* **101**, 045415 (2020).
- [55] S. Weidemann, M. Kremer, S. Longhi, and A. Szameit, Topological triple phase transition in non-Hermitian Floquet quasicrystals, *Nature (London)* **601**, 354 (2022).
- [56] C.-H. Liu, H. Hu, and S. Chen, Symmetry and topological classification of Floquet non-Hermitian systems, *Phys. Rev. B* **105**, 214305 (2022).
- [57] W. Zhu and J. Gong, Hybrid skin-topological modes without asymmetric couplings, *Phys. Rev. B* **106**, 035425 (2022).
- [58] S. Ke, W. Wen, D. Zhao, and Y. Wang, Floquet engineering of the non-Hermitian skin effect in photonic waveguide arrays, *Phys. Rev. A* **107**, 053508 (2023).
- [59] H. Gao, H. Xue, Z. Gu, L. Li, W. Zhu, Z. Su, J. Zhu, B. Zhang, and Y. D. Chong, Anomalous Floquet non-Hermitian skin effect in a ring resonator lattice, *Phys. Rev. B* **106**, 134112 (2022).
- [60] See Supplemental Material at <http://link.aps.org/supplemental/10.1103/PhysRevB.108.L220301> for the effective coupling matrix, phase diagrams, projected band structures and non-Hermitian Chern numbers of typical examples.
- [61] X. Huang, C. Lu, C. Liang, H. Tao, and Y.-C. Liu, Loss-induced nonreciprocity, *Light: Sci. Appl.* **10**, 30 (2021).
- [62] Y. Sun, X. Hou, T. Wan, F. Wang, S. Zhu, Z. Ruan, and Z. Yang, Photonic Floquet skin-topological effect, [arXiv:2306.03705](https://arxiv.org/abs/2306.03705).